CMS DN giunta_001

The Compact Muon Solenoid Experiment

Detector Note

The content of this note is intended for CMS internal use and distribution only

2012/11/03
Head Id: 155750
Archive Id: 156366
Archive Date: 2012/10/31
Archive Tag: trunk

Feasibility study of a Fused Quartz detector for measuring the Machine Induced Background in the CMS Cavern

M. J. Ambrose[2], A. E. Dabrowski[1], M. Giunta[1], S. Orfanelli[1], R. Rusack[2], and D. Stickland[3]

[1] CERN CH-1211 Genève 23, Switzerland
[2] University of Minnesota, 116 Church Street S.E, Minneapolis, MN 55455, USA
[3] Princeton University, Princeton, NJ 08544-0708, USA

Abstract

The CMS Beam and Radiation Monitoring (BRM) group is responsible for monitoring the beam induced background in the CMS cavern. At the present LHC luminosities and 50 ns bunch spacing, beam gas and beam halo events at large radius are measured using the Beam Halo Counters (BHC) [1] system, a scintillator based detector. Owing to an insufficient dynamic range and time resolution, this detector will unfortunately not be able to efficiently monitor beam backgrounds for the present LHC parameters and beyond. Hence an upgraded detector is required, to be operational after "Long shutdown 1" (LS1). The feasibility of monitoring this large radius beam induced background radiation, by detecting Cherenkov light produced in fused quartz, is investigated in this note.

1 Introduction

Monitoring the quality and the stability of the LHC beam in the proximity of the interaction point is important to ensure high quality physics data-taking. The presence of a high flux of particles parallel to the beam, coming from the tunnel, is symptomatic of degraded beam conditions. The source of this ”machine-induced” background (MIB) is either muon halo particles, produced by interactions of beam halo LHC protons with collimators located at about 150 m from the CMS interaction point or beam gas events originating from interactions in the vacuum chamber of primary protons with residual gas atoms [2] [3] [4]. Beam diagnostics are hence needed for online monitoring, to provide real-time feedback to the LHC operators and CMS experimental shift crew.

The machine-induced background at low radius (r = 4.5 m) and close to the interaction region (Z = ±1.8 m) has been measured since first LHC beams using the BCM1F detector [5]. This detector, with its foreseen front-end electronics upgrade during LS1, will continue to provide monitoring after LS1. At higher radius, during the first years of running of LHC at low luminosity (2009-early 2011) the beam background was measured using the Beam Scintillator Counter (BSC) detector [6]. At a luminosity of about $2.5 \times 10^{32}\,\mathrm{cm}^{-2}\,\mathrm{s}^{-1}$, as expected, the detector went into saturation. During the 2011-2012 winter technical break a new scintillator-based detector system was installed, called the ”Beam Halo Counters” (BHC) to measure at intermediate luminosities and 50 ns bunch spacing, expected in 2012. This detector was mounted at the same longitudinal position as the BSC, $z = \pm\,10.9$ m from the Interaction Point (IP), and a radius of about 1 m and hence sensitive to beam gas and beam halo events at large radius. Unfortunately, at nominal and above nominal luminosity, the BHC too will saturate. The intrinsic time needed to produce and measure the scintillation light using the BHC, is also too long when compared with the 25 ns bunch spacing. In addition, its longitudinal z location position is not optimized to separate beam background from collision products based on arrival time information. The higher level of integrated radiation foreseen after LS1 is expected to damage the scintillating material, making it opaque and less efficient, and eventually unusable.

For these reasons, the BRM group has a mandate to design a radiation-hard, fast, MIB-sensitive detector system, capable of monitoring at nominal LHC luminosity and the beam conditions expected between LS1 and LS2. This detector note studies the feasibility of using a quartz-based device for beam halo detection in the CMS cavern. This technology has the potential to be fast, radiation-hard and sensitive to only charged particles, making it attractive for this application.

Two main principles for optimising the muon halo detection and reducing the relative background contribution from collision products are driving the research and design efforts:

- *Timing*: the detector location is chosen in order to maximize the time difference between incoming beam and outgoing beam/collision products (see Fig. 1). This condition is met when the distance from the CMS IP is equal to $(12.5 + n \cdot 25)\,ns$ (where $n = 1, ..., 7$). These particular locations are called *Golden Locations* (GL) and are shown in Fig. 2. This naive calculation is valid in the regime that that the azimuthal angle to the z-axis is small and that timing corrections due to multiple scattering are small. This is certainly valid for detectors positioned close to the beam pipe. Simulation is needed to correct this assumption for detectors placed at larger radius and behind heavy material.
- *Directionality*: with this term we mean the property of the detector to distinguish between particles coming from different directions and the consequent capability

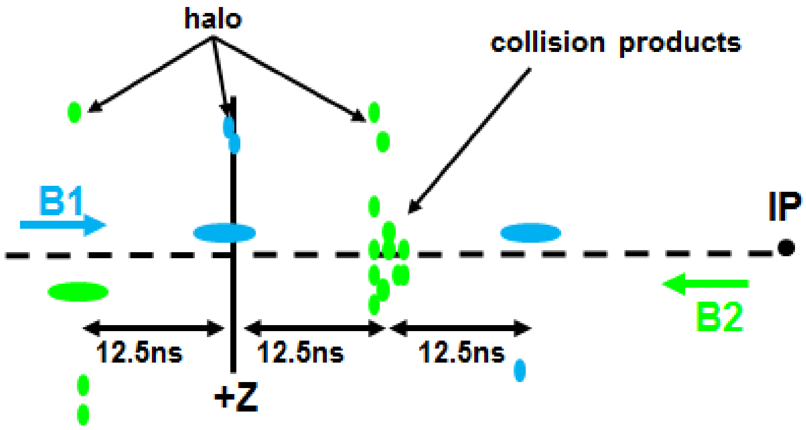

Figure 1: Cartoon showing the optimal time separation between incoming and outgoing particles achievable in the Golden Locations.

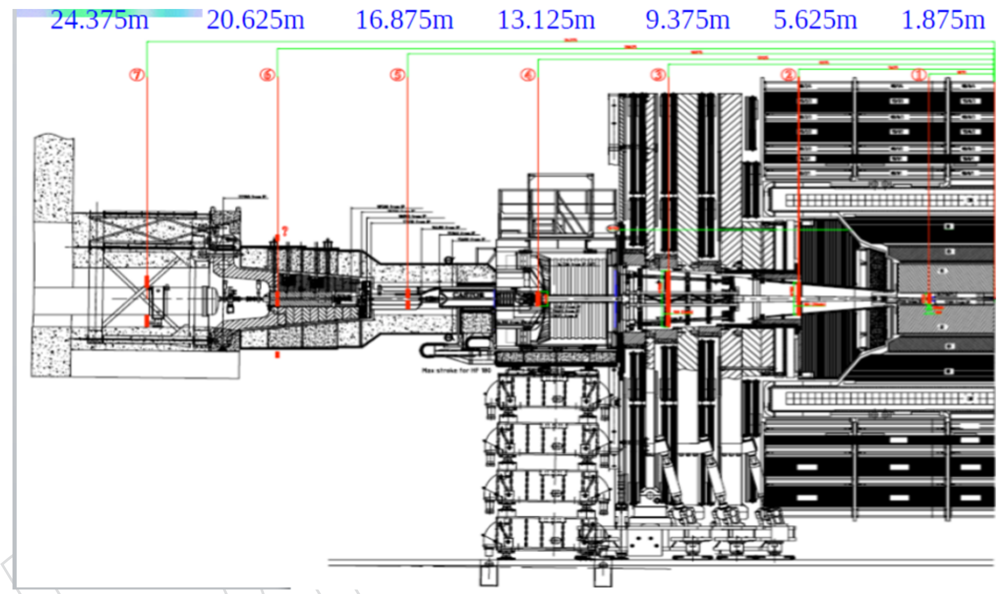

Figure 2: Schematics of the $+Z$ side of the CMS detector showing the distance from the interaction point of the seven so called *Golden Locations*

to suppress background signal, while preferentially selecting particles parallel and consistent with the direction of the incoming beam. A device based on the detection of Cherenkov light produced by a charged particle crossing a suitable material has this important feature.

The note is organised as follows: In Section 2, the environmental challenges in the CMS cavern foreseen after the Long Shutdown 1 (LS1) are reviewed. In Section 3, the nominal expected machine induced background fluxes and particle spectra are described as well as the "background particle" distributions expected from collision products. The impact of the CMS environment and the expected particle flux distributions define the detector requirements, which are presented in Section 4. Then, some of the advantages of using fused quartz as the Cherenkov medium are described in Section 5, and results from a test beam carried out at the PS T9 area between the 2^{nd} and 9^{th} of July 2012 to validate the technology choice are presented in Section 6. In Section 7, a possible integration scenario of the detector into the CMS cavern is reviewed, and finally in Section 8, an outlook on future work needed in order to optimise the design is given.

2 CMS Cavern Environment

Two important environmental properties influence the location choice and the design of the new detector:

- *Radiation Dose*: the location is selected in order to minimize the level of radiation absorbed by the device during its life-time; the material and possible on-detector electronics have to be chosen such that their performances do not significantly deteriorate with time.
- *Magnetic Field*: a good knowledge of the magnetic field is important in the choice of the photo-detector used and its location since Photo Multiplier Tubes (PMT) are highly sensitive to its magnitude and direction.

Simulated results obtained with FLUKA [7] [8] (for the radiation dose) and Opera [9] (for the magnetic field) are presented in the following paragraphs.

2.1 Radiation dose

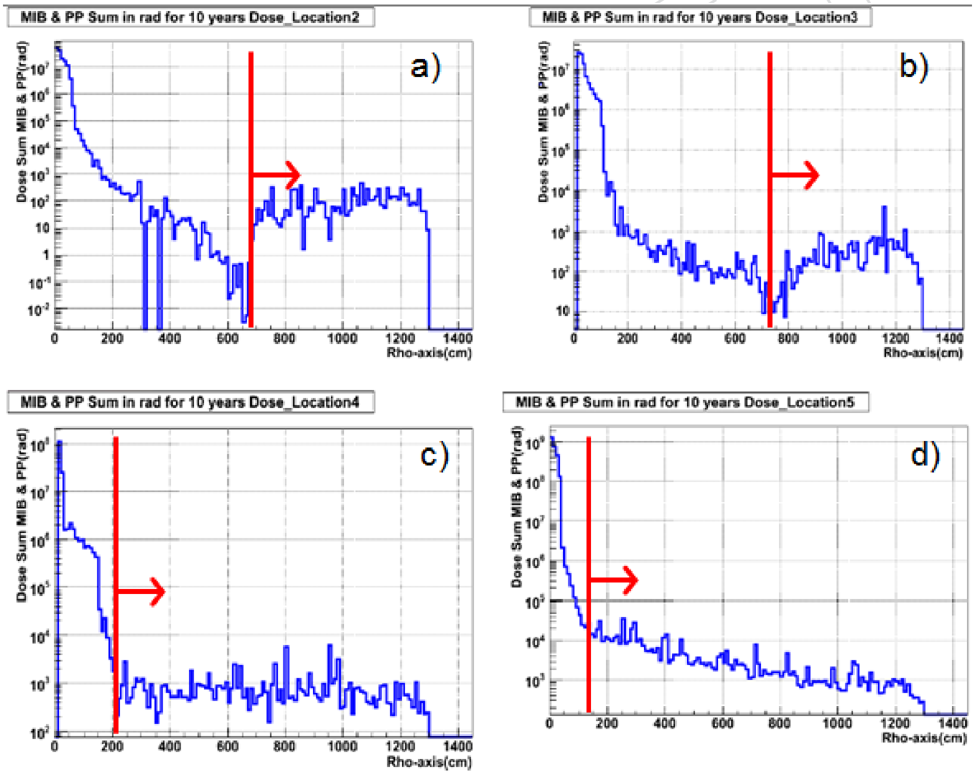

Figure 3: Radiation dose in GLs 2 to 5 as a function of the radial distance from the beam pipe.

FLUKA simulated events [10] both for pp collisions and Machine Induced Background (MIB) are post-processed and used for the evaluation of the radiation dose in the interesting GLs. For the MIB, input files produced with MARS [11]are used, and then propagated into the CMS cavern using Fluka. The interface plane is at 22.6 m from the IP and the hits in the LHC Tertiary Collimators (TCT) are simulated using SixTrack [12].

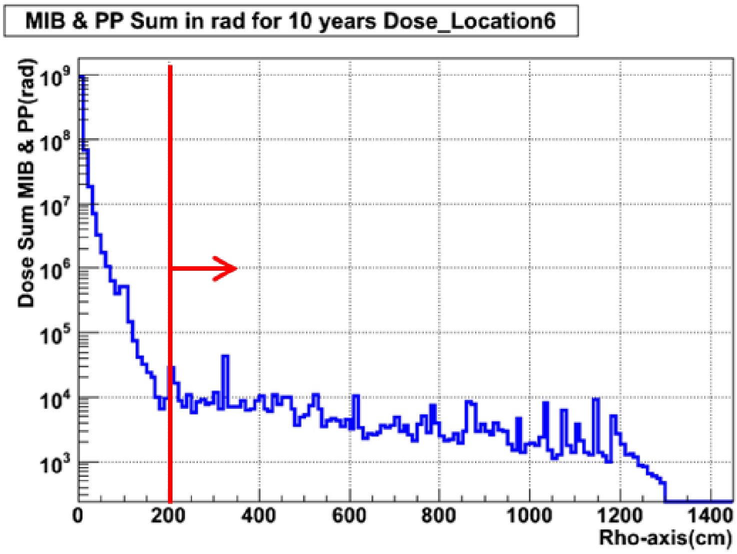

Figure 4: Radiation dose in GL6 as a function of the radial distance from the beam pipe.

The radiation dose is evaluated in six out of the seven GLs because the seventh location (at 24.375 m from the IP) is beyond the interface plane and is not covered in this simulated sample. Results for ten years of LHC operations (180 days/year, average $\mathcal{L} = 10^{34}\,\mathrm{cm}^{-2}\,\mathrm{s}^{-1}$) are shown in Fig. 3 for GLs 2 to 5 and in Fig. 4 for GL 6. GL6 is considered the preferred installation location, see Section 3.1. The regions indicated by the red arrows are those available (i.e. free space) for the installation of the new detector array. It can be noticed that the dose quickly decreases with radius and in the regions of interest it usually goes down to values between $10^2\,rad$ and $10^4\,rad$, expected to produce no significant damages in fused quartz.

2.2 Magnetic Field

The strength of the magnetic field ($\vec{B}$) in the GLs was simulated using the Opera [9] tool. Since we are considering locations placed outside the CMS yoke, the magnetic field is in general quite low. In Fig. 5, the longitudinal and radial components of $\vec{B}$ as a function of the distance from the beam pipe are shown for GL6. The magnitude of the field in each direction is always below 200 gauss. The presence of a strong $\vec{B}$ field can be a problem, especially for the photodetector device, but a field of this magnitude can be easily shielded using magnetic shield cases.

3 Comparison of particle distributions in beam halo events and pp collisions

In order to optimize the acceptance and granularity of the detector, a detailed study of the properties of the particles coming from signal (MIB) and background events (pp collisions) is needed. For this reason new FLUKA simulations were produced and, for each particle, the information about energy, direction and time of arrival at the plane perpendicular to the beampipe, located at the z value of each GL, was saved.

3.1 Particle fluxes, directions, energies in interesting locations

A particle will produce Cherenkov light in a material when the condition $\beta > 1/n$ is satisfied, where $\beta = v/c$ is the particle velocity in the medium and n is the index of refraction of the

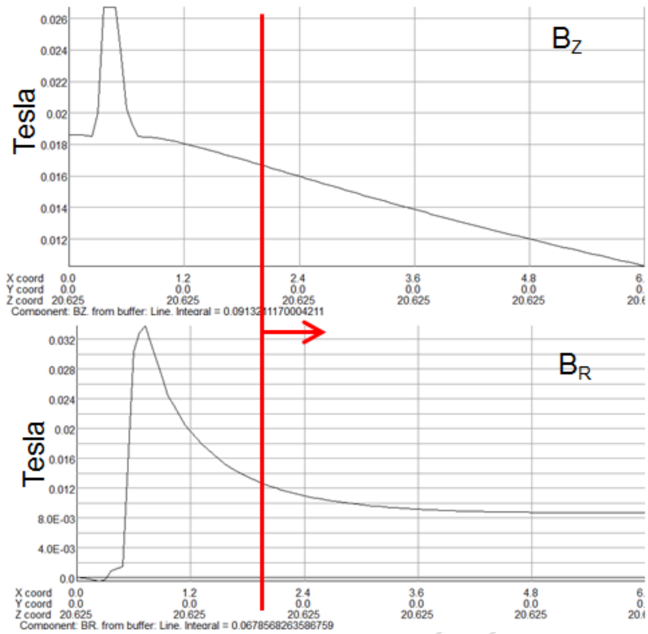

Figure 5: Magnetic Field in GL6: longitudinal (Top) and radial (Bottom) component.

material. Hence, the energy threshold for which this condition is met depends on the index of refraction of the material and the particle type. In the new FLUKA simulations, in order to save information only for those particles able to produce Cherenkov radiation in fused quartz, we considered the refraction index of the reference material for this study (HSQ300 from Heraeus [13]) and hence the following threshold energy cuts were applied in the final scorings of the changed particles:

- e: 190 keV
- μ: 39 MeV
- p: 350 MeV
- π: 52 MeV
- K: 185 MeV

For the particles above the energy threshold, we scored the following information:

- detailed list of variables scored (only those that we actually use) from Stella (Note To All: Need to fill in this list)

First of all, we selected the Golden Location giving the best result in terms of MIB total flux and ratio of MIB to pp fluxes (for charged particles capable of emitting Cherenkov radiation). Results are summarized in Tab. 1. From the table it can be noticed that a reasonably good MIB flux ($\sim 1 \mathrm{H}^0/\mathrm{cm}^2$) is present in GL5 and GL6, the last one having the best flux ratio. For this reason GL6 is the favourite choice; the relevant plots for GL6 are shown in Fig. 6. Then, we studied other important properties of the particles reaching GL6 (i.e. crossing the plane perpendicular to the beam pipe at $z = 20.625m$): angle, energy and time distributions.

Golden Location	Z (m)	Min Ratio	Max Ratio	MIB Flux (cm^2/s)
2	5.625	10^{-4}	10^{-4}	0.001-0.01
3	9.375	10^{-2}	10^{-2}	0.001-0.01
4	13.125	10^{-4}	10^{-2}	0.001-0.1
5	16.875	10^{-4}	10^{-4}	0.001-1
6	20.625	10^{-4}	10^{-3}	0.001-1

Table 1: Flux ratios and MIB total flux in the GL. (Note To Stella: If you keep this table, mention all charged particles (no Cherenkov threshold that castor is in the geometry)) (Note To Stella: Better to make a new table without castor and with the Cherenkov threshold applied)

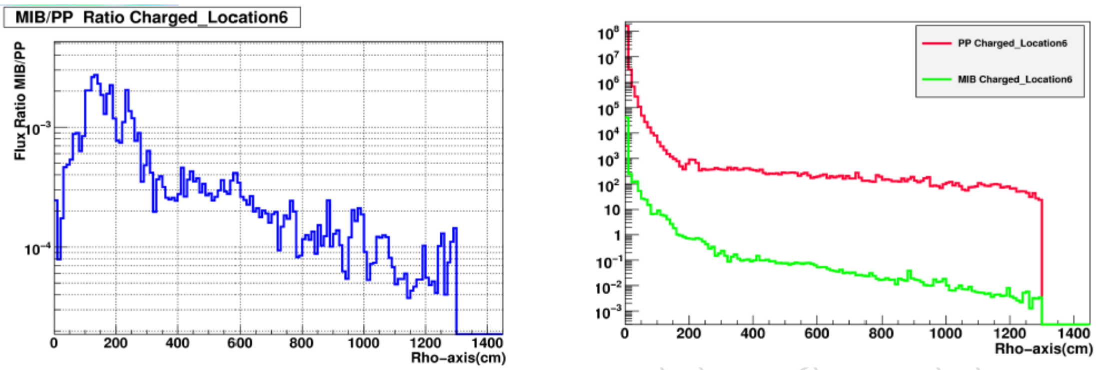

Figure 6: Particle flux in GL6 due to MIB and pp collision. Ratio (Left) and total values (Right) as a function of the radial distance from the beam pipe.(Note To Stella: Steffens results, old geometry, old magnetic field, and no castor ... so must update)

We only considered particles crossing the plane at a radial distance between 2 m and 3 m from the beam pipe, since this is the most interesting available region for installation (simulations show that the flux of MIB particles from the tunnel starts to decrease above that value). The angular distribution at the scoring plane of both forward and backward particles is of primary importance for optimizing the position of the detector; in fact its inclination with respect to the beam pipe direction will be chosen in order to minimize the forward signal rejection for a given backward signal acceptance. These FLUKA results will be used as input for the direction and energy of incident particles in a GEANT4 simulation of the fused quartz bar response, described in Section 6.3.

In Fig. 7, two dimensional plots of the angular and energy distributions of muons crossing $GL6$ from MIB and pp collisions are shown. The zero degree angle corresponds to particles going from the IP to the tunnel. From these plots it is clear that we can easily separate muons coming from MIB from the background ones. Evaluating the time distributions of the background particles is also important to understand if we can rely on a time separation between signal and background and use it to gate only on the incoming (MIB) signal and reject the rest. In Fig. 8, an example is shown.

3.2 Background shielding

FLUKA simulations show that the average MIB flux of particles arriving from the tunnel in GL6 in the region of interest (i.e. between 2 m and 3 m from the beam pipe) is $\sim 0.4\ particles/cm^2/s$

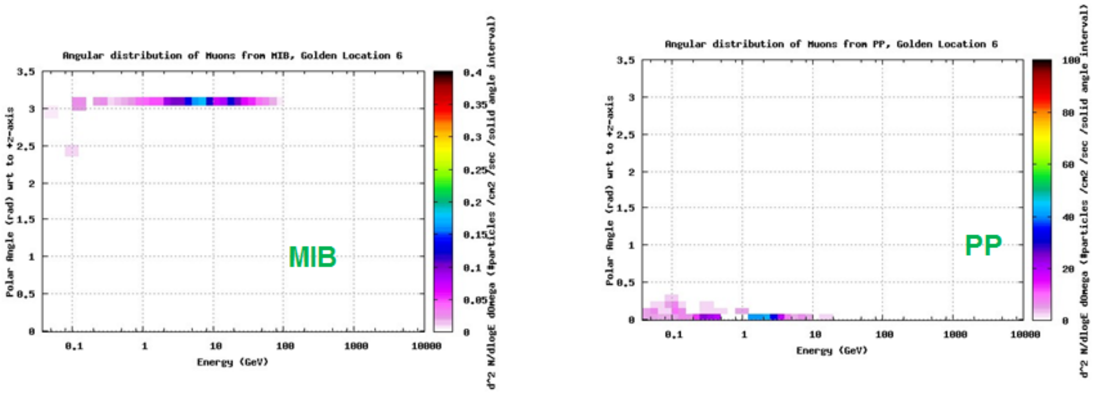

Figure 7: Two dimensional histograms showing the angular vs. energy distribution for MIB muons (Left) and muons coming from pp collisions, passing the Cherenkov threshold

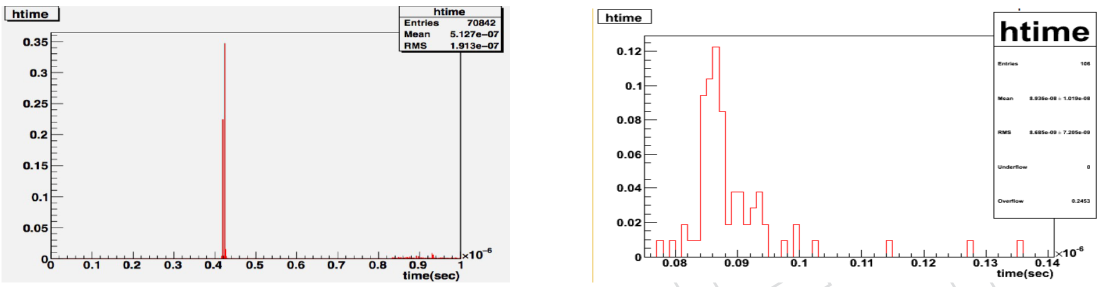

Figure 8: Time distribution for background particles (Left) and particles coming from pp collisions (Right).

(mainly muons), while $\sim 45\, particles/cm^2/s$ (electrons and positrons) produced in pp collisions are expected to come from the same direction (i.e. from the tunnel towards the IP) and produce a fake signal in the bar completely undistinguishable from the MIB we want to measure. We also consider photon background present in the cavern, since energetic photons can create delta rays capable of producing Cherenkov radiation in the bar generating a fake signal. Fig. 9 shows the energy spectrum of the photons reaching GL6.

In order to reduce the fake signal rate, the quartz bars need to be enclosed in an appropriate support capable of shielding $e^{\pm}$ and photons without production of secondary particles from interaction with the shielding material itself. A suitable choice seems to be a box made of 10 mm thick aluminum.

From Fig. 10(Left), showing the energy distributions for $e^{\pm}$ coming from pp collisions, one can conclude that less than 10% of those coming from the tunnel direction have energy above 10 MeV. Fig. 10(Right) shows the number of photoelectrons produced in the PMT by a 10 MeV electron after passing a 10 mm thick aluminum plate compared to the reference signal (in black) for a 6 GeV muon; the electron signal is much lower and well separated (without any overlap) from the muon distribution. From these plots it's clear that such a plate is enough to reduce this type of background by 90%. Fig. 11 shows similar plots for 10 MeV (Left) and 100 MeV (Right) photons. The first ones will be completely absorbed, while the second ones will produce a flat distribution up to values that can generate a fake signal. However, given the energy distribution in Fig. 9.......
(Note To All: Need to finish this section).

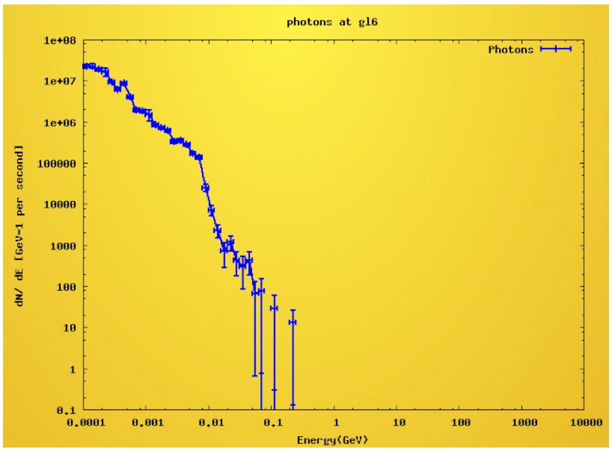

Figure 9: Photon energy distribution

4 Detector Requirements

Given the LHC conditions foreseen after LS1 (expected peak luminosity $\sim 2x10^{34}$ and 25 ns bunch spacing) and the need for this detector to monitor MIB as soon as the first bunches are injected in the ring, the following requirements must be met:

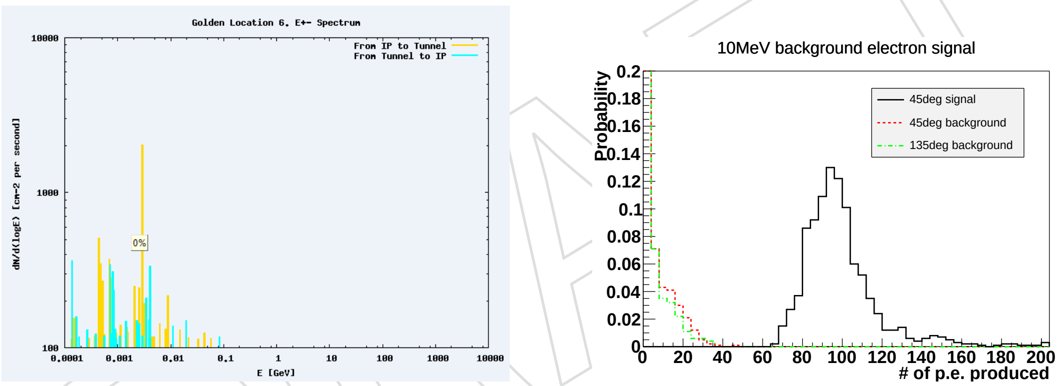

Figure 10: The expected energy distribution of electrons from pp collisions (Left) and the number of photoelectrons produced in the PMT attached to a quartz bar by 10 MeV electrons after crossing a 10 mm aluminum plate (Right).

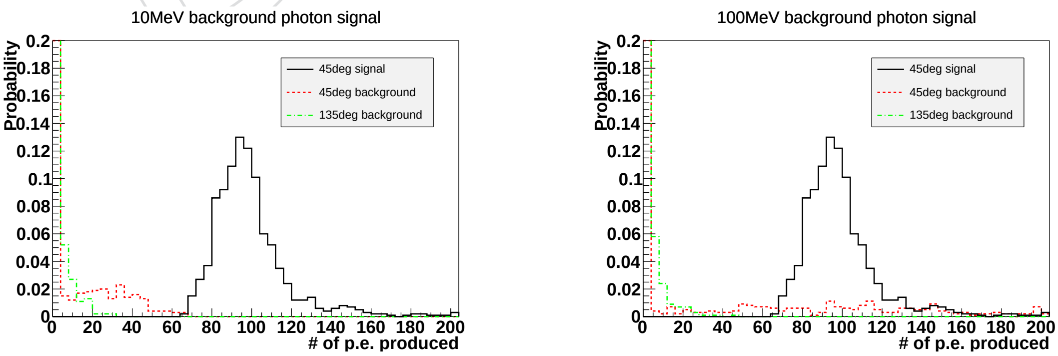

Figure 11: The number of photoelectrons produced in the quartz bar by 10 MeV photons (Left) and 100 MeV photons (Right) after crossing a 10 mm aluminum plate

- Fast Time Resolution ($< 12\,$ns): in order to separate incoming beam background from collision products with the 25 ns bunch spacing
- Radiation Hardness and insensitivity to γ and thermal neutrons: these particles are the main background present in the CMS cavern
- Granularity and Acceptance: the detector should cover an area of at least $250\,cm^2$ in each side in order to have an acceptable rate given the MIB and background particle fluxes expected in GL6 (see Section 3.2). When considering fused quartz bars with a diameter of 30-45 mm, this corresponds to between 20 and 40 channels (depending on the bar section) per side
- Readout independent of CMS DAQ: must operate whenever there is beam in the machine, even if the central CMS experiment is not taking data
- Cost: the detector must be designed and built with a limited budget

Given the fact that a *directional* detector is needed, in order to suppress the high pp background and the demanding time resolution constraint, a device based on Cherenkov light detection seems the most suitable.

5 Advantages of using fused quartz

In order to maximize the Cherenkov signal for particle coming from the preferred direction, a material with the following properties is needed:

- a good Cherenkov light production when crossed by relativistic charged particles
- a low scintillation radiation component, since it is isotropic and would spoil the directionality of the detector
- radiation hard
- transparent
- cost-effective

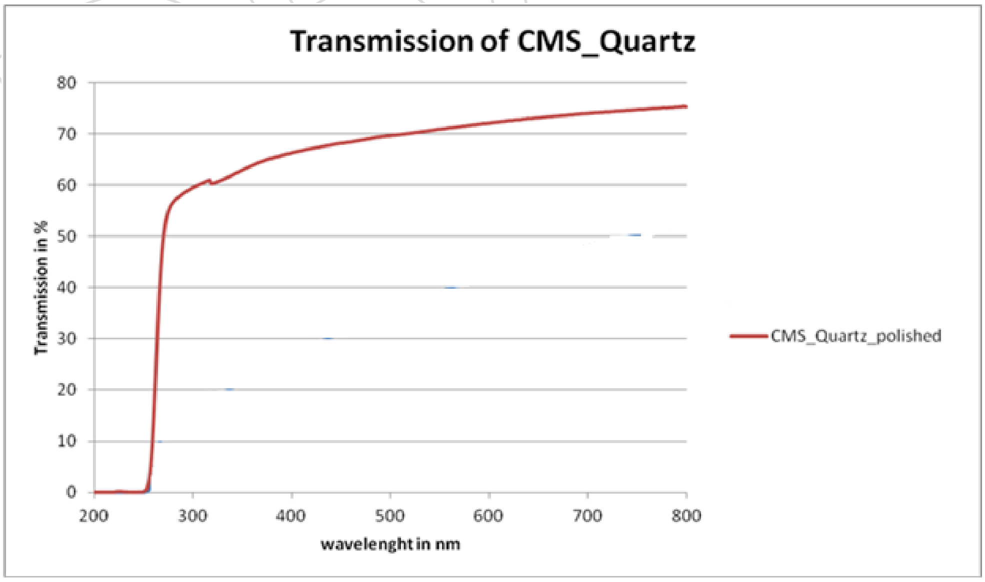

Figure 12: Transmission curve of a 20cm long HSQ300 bar. [1]

The properties of three different types of material were examined[14]: fused quartz, fused silica, and sapphire. Parameters that influence the production of Cherenkov light (refractive index), transmission of light (density), radiation hardness and the possibility of having it in the desired shape were investigated.

Sapphire has an excellent radiation hardness and a higher index of refraction ($\sim$1.78 at 420) than fused silica or fused quartz ($\sim$1.47 at 420), so it produces more Cherenkov photons, but because of its high density ($\sim$ 3.98 g/cc) it has a high attenuation above 1 mm thickness, so the collected light for a bar of the size being considered (10-20 cm) is very low. Moreover, it is quite expensive and not easy to have in any desired shape.

Fused quartz and synthetic fused silica seem to have the needed optical properties, with the first one being less expensive. Given this, preliminary tests were performed, to check the time resolution and directionality of Cherenkov light, with a fused quartz bar produced by Heraeus [13] (HSQ300). Precise information about the radiation hardness of this material was not found, hence a radiation test with a 100 krad dose is foreseen in the next month. Fig. 12 shows the transmission curve measured for a 20 cm long bar of this material.

6 Validation of the technology

6.1 Test beam setup

The directionality property of the Cherenkov light produced in the fused quartz cylinder and measured by the photodetector was studied in a test beam carried out at the CERN East Area [15] [2].

6.1.1 Test beam parameters

The T9 beam line was used, allowing data to be taken with both muons and protons. A $\sim$4 GeV muon beam was obtained by selecting a 6 GeV secondary beam. For the proton runs, data was collected with a 9 GeV beam since at that energy the beam has the highest proton purity ($\sim$ 50%); a further reduction in the pion contamination was obtained by using the gas Cherenkov counters present in the T9 line. The beam was focused at the center of the cylinder. The proton beam had a r.m.s. cross sectional diameter of approximately 10-15 mm, while the muon beam had a much larger size ($\sim$40 mm) since collimating the muons was not possible.

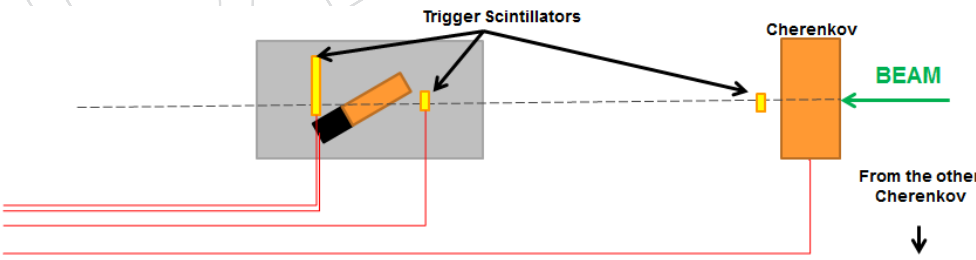

Figure 13: Sketch showing the test beam set-up

6.1.2 Trigger and DAQ

The coincidence of three scintillator counters, as shown in Fig. 13, was used as external trigger. The analog signal corresponding to the photons produced in the fused quartz bar, each of the

[2]We would like to thank the people who helped us to set up and carry out the test beam: A. Finkel, A.K. Mukherjee, S. Nag, S. Singovski, R. Zuyeuski.

two scintillators closest to it and the digital signal from the trigger coincidence were all sent to a *LeCroy Waverunner 104 Mxi* oscilloscope used for the acquisition, set in order to acquire data in *Sequence* mode with a 1 ns resolution. A rate of 50 Hz per spill was achieved for the muon beam, where the limiting factor was the small area covered by one of the trigger scintillator (15 mm x 15 mm). The rate for the proton beam was .... (Note To Marina: maybe can check with Lau?)

6.1.3 Measurement program

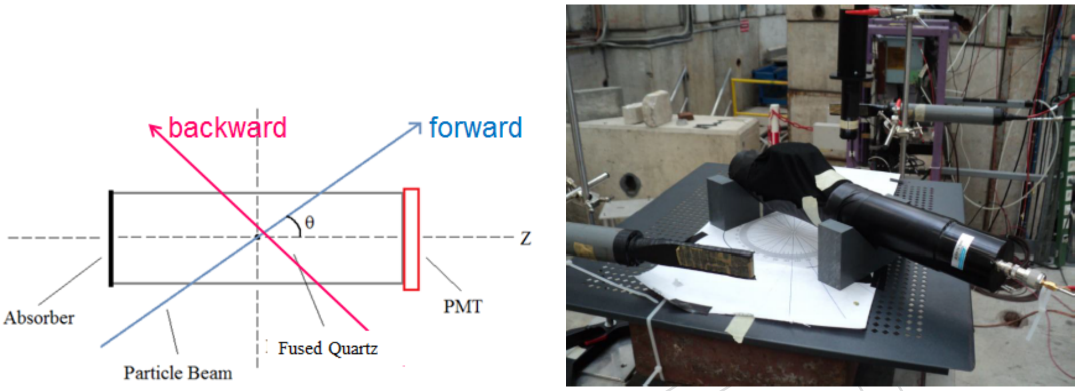

Figure 14: Sketch showing the definition of *forwards* and *backwards* primary particle angles with respect to the PMT position (Left). Picture of the detector during the test beam (Right).

In order to verify the suppression of the collected Cherenkov light for a relativistic particle crossing the bar pointing in the direction opposite to the photodetector (*backward* direction), data were collected with the beam hitting the bar at different incident angles. Fig. 14 (Left) shows a sketch of the detector and the definition of *forward* and *backward* directions (for example $\theta = 150$ degrees is equivalent to 30 degrees *backward*); in Fig. 14 (Right) you can see a photograph of the experimental setup and detector setup tested during the test beam. The light produced in the bar was collected by a *Hamamatsu R2059* photomultiplier tube operated at 2000V. Data was collected at $\theta = 0, 15, 30, 45, 60, 90$ degrees (*forward* and *backward*). Samples of 10k events were acquired for the *forward* measurements and 100k events for the *backward* directions.

The signal from the quartz bar varied significantly with the incident angle; in some cases one to four 3dB attenuators had to be added in order not to have a saturated signal. Muon data was collected with three different quartz bars: a 20 cm long bar with both ends polished, another 20 cm long bar with one end painted black (used also for proton runs), a 10 cm long bar blackened at one end. Data was also taken without a bar, with the PMT window directly in the beam line.

6.2 Test Beam Results

The analysis of the test beam data was focused on answering the following questions:

- What is the directionality of Cherenkov signal as a function of incident beam angle?
- What are the timing characteristics of the Cherenkov signal?
- What are the possible reasons for the large signals observed at low beam angles?

The remainder of this section will address each of these questions in this order.

6.2.1 Directionality

Fig. 15 displays an example of typical forwards and backwards PMT waveforms produced by relativistic muons passing through the quartz cylinder. The stark amplitude difference between the forwards and backwards waveforms gives a good qualitative indication of the directionality of the Cherenkov radiation produced in the quartz. Nevertheless, there is a population of backwards waveforms which reach amplitudes comparable to some of the smaller forwards waveforms. To determine the extent of this overlap, a quantitative directionality metric needed to be developed.

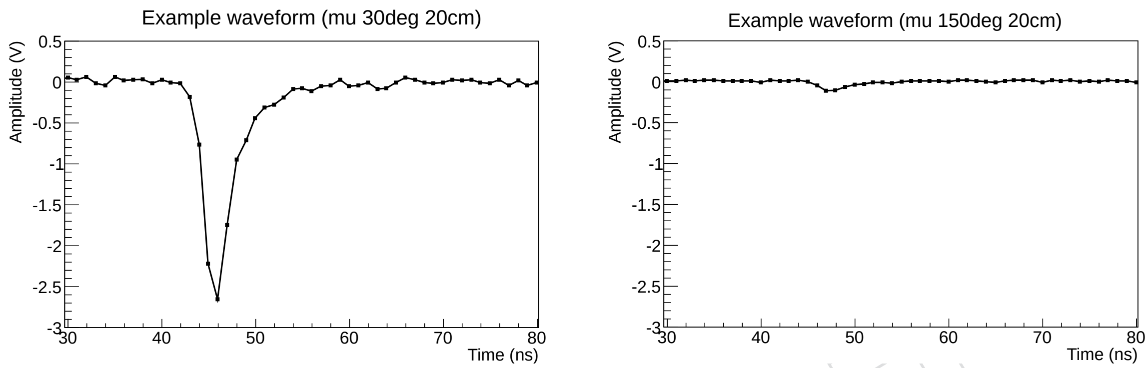

Figure 15: Typical PMT waveforms produced by a relativistic muon passing through the 20 cm quartz cylinder at 30 degrees (Left) and 150 degrees (Right).

A straightforward way of quantifying the directionality of the Cherenkov signal is to determine the degree of overlap between histograms of the maximum amplitude of the waveform, since a voltage threshold will be used to discriminate the signals. However, partially due to the fact that much larger than expected signals were observed, in the data collected some of the recorded waveforms exceeded the range of the oscilloscope and thus the maximum amplitude information for these waveforms was lost. Although this only occurred for a small number of waveforms (typically around 0.1% of the total), this is nevertheless a significant number if one is trying to make conclusions about effects which occur in less than 1 out of 1,000 events. One possible solution to this problem is to fit the main peak in each waveform that went out of bounds (ignoring the saturated data points) in order to reconstruct the maximum amplitude. Another possible solution is to make a histogram of the waveform amplitude a few nanoseconds after the time at which the maximum voltage was reached. Assuming that the shape of the falling edge of the peak is relatively constant, this value is proportional to the maximum voltage.

Both of these options were pursued, and ultimately the latter proved to be more reliable. Fig. 16 shows an example of this type of overlay. Like Fig. 15, Fig. 16 offers another striking depiction of the directionality of the Cherenkov signal. The extent of overlap is such that it is only visible in logarithmic scale. Overlay histograms such as this one can be used to determine what will be referred to as the "forwards signal rejection" and the "backwards signal acceptance" as a function of discrimination amplitude. The forwards signal rejection at a voltage X is the percentage of Cherenkov pulses produced by forwards moving particles that would be rejected if the discriminator was set to that voltage. Similarly, the backwards signal acceptance at a voltage X is the percentage of Cherenkov pulses produced by backwards moving particles that would be confused as Cherenkov pulses produced by forwards moving particles if the discriminator was set to that voltage.

Fig. 17 shows what will be referred to as a "detection efficiency overlay," and was constructed

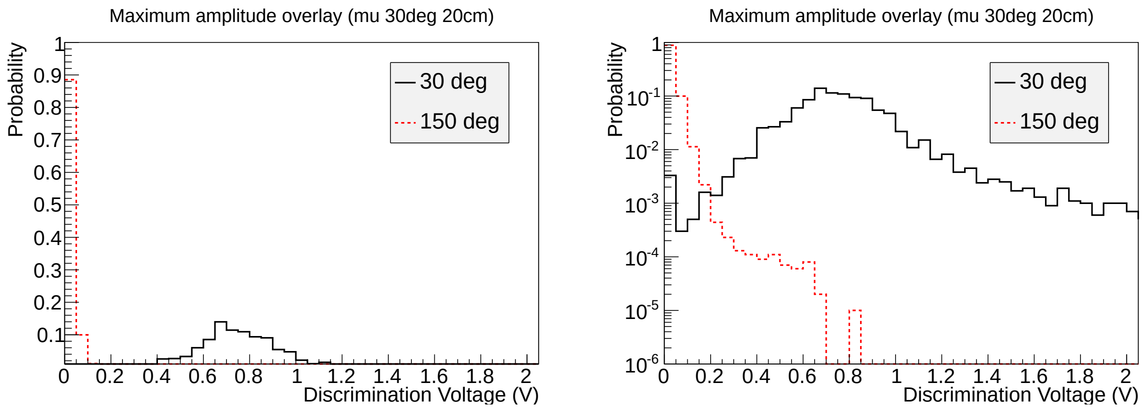

Figure 16: Histogram overlays in linear (Left) and logarithmic scale (Right) of all waveform amplitudes 3 ns after the maximum amplitude for relativistic muons incident on the 20 cm quartz cylinder at 30 and 150 degrees.

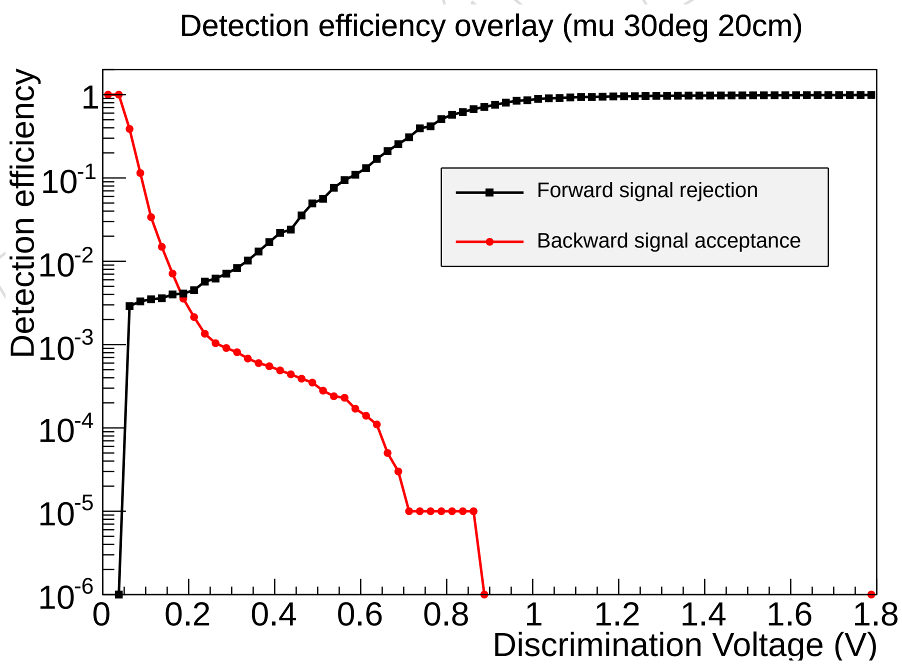

Figure 17: Backward signal acceptance and forward signal rejection efficiency as a function of discrimination amplitude for a forward beam angle of 30 degrees paired with a backward beam angle of 150 degrees.

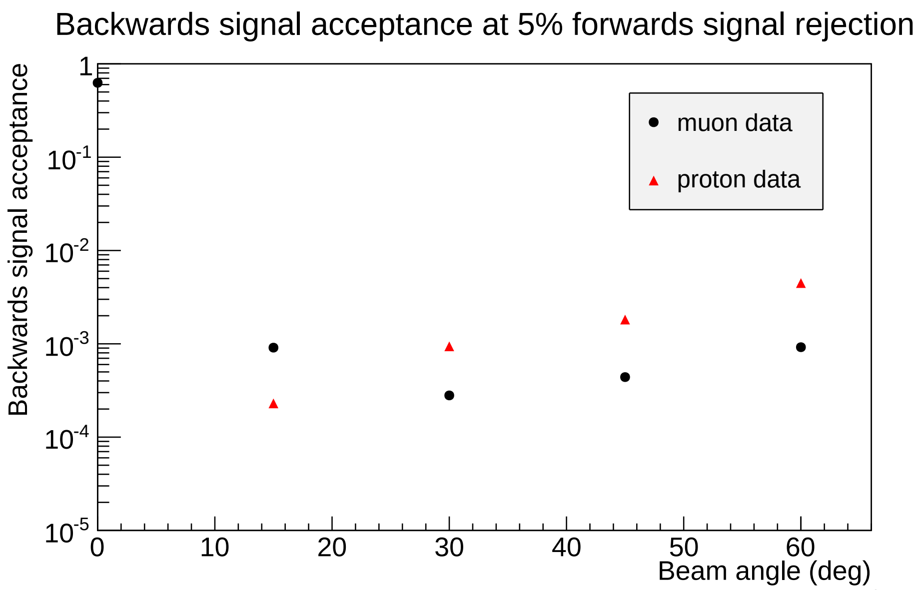

Figure 18: Backwards signal acceptance at 5% forwards signal rejection as a function of beam angle for relativistic muons and protons passing through the 20 cm fused quartz cylinder. Each angle is paired with its supplementary angle (e.g. 30 is paired with 150 and 45 is paired with 135). No data was collected for a 0 degree proton beam.

using the data in Fig. 16. Beginning at a discrimination voltage of 0 V, 100% of the backwards signal is accepted and 0% of forwards signal is rejected. As the discrimination voltage is increased, the backwards signal acceptance decreases at the expense of an increase in the forwards signal rejection. Note that a backwards signal acceptance efficiency of 10ˆ-3 means that 1 out of 1,000 backward moving particles (e.g. pp collision products) would be confused as forward moving particles (e.g. machine induced background). One way to compare the detection efficiency overlays of different beam angles is to set the discrimination voltage such as to achieve a fixed forwards signal rejection and then record the corresponding backwards signal acceptance.

Fig. 18 plots the backwards signal acceptance at 5% forwards signal rejection as a function of beam angle for muons and protons incident on the 20 cm quartz cylinder. The particularly poor directionality of the detector at 0 degrees will be explained later in section 6.2.3. The 0 degree data point aside, this plot demonstrates that 1) for a relatively small loss of forwards signal, backwards signal acceptances of less than 0.1% are readily achievable, 2) there is a slight correlation between backwards acceptance efficiency and beam angle and 3) the response of the detector for muons and protons is comparable.

No unexpected differences were observed between data sets taken with different quartz cylinder lengths. The two quantities that are sensitive to a change in cylinder length are the path length of the primary particles through the material and the path length of the Cherenkov photons through the material. For low beam angles, the primary particles will pass through more material for longer cylinders as compared with shorter cylinders, whereas for higher beam angles, the particles will have a path length solely determined by the cylinder radius. Thus the amount of Cherenkov photons detected should be independent of cylinder length for sufficiently high beam angles with the exception of the differences resulting from the increased chance of photon absorption within longer cylinders. This greater chance of photon absorption is simply due to the increased path length of the Cherenkov photons, but overall, differences in

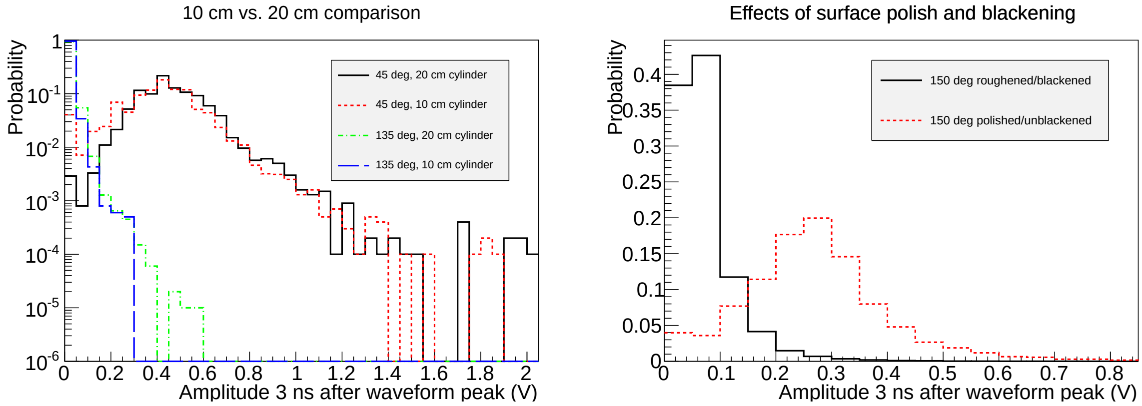

Figure 19: Comparison of data collected with quartz cylinder lengths of 10 and 20 cm (Left) and polished/unblackened versus roughened/blackened cylinder end-faces (Right).

photon absorption should be minor for the lengths under consideration. The left plot in Fig. 19 demonstrates this lack of difference between the data collected with the 20 and 10 cm length cylinders at high beam angles.

On the other hand, a significant difference was observed (as expected) for *backward* beam angles between the data collected with the end surface of the quartz cylinder opposite the PMT polished/unblackened and the data collected with the end surface roughened/blackened. The right plot in Fig. 19 demonstrates this difference, which can most likely be attributed to the greatly increased probability for Cherenkov photons to reflect off the unblackened end surface of the cylinder and potentially reach the PMT. It is not however obvious what effect the end surface roughness has on the directionality. A roughened surface will smear the angular distribution of the reflected photons whereas a polished surface will not affect the angular distribution. This angular smearing may not necessarily improve the directionality, as one might initially assume. Nevertheless, the surface roughness should be far less important than the blackening in influencing directionality. The main takeaway from this plot is that the observed differences indicate the importance of carefully designing the cylinder end surface such as to minimize the probability of photon reflection.

6.2.2 Timing Characteristics

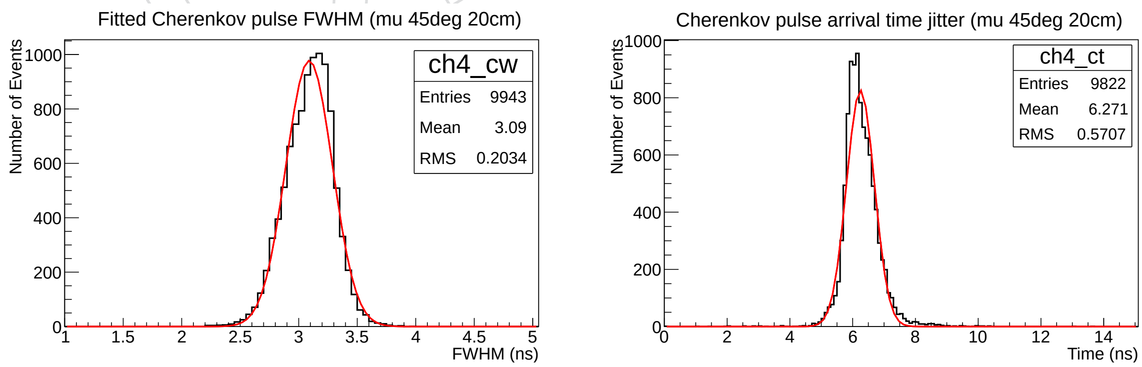

Figure 20: FWHM of main peak (Left) and signal arrival time jitter (Right) for 10,000 relativistic muons passing through the 20 cm quartz cylinder at 45 degrees.

In addition to discriminating based on signal amplitude, one would hope to also be able to discriminate on timing information in order to further improve the ability to differentiate in-

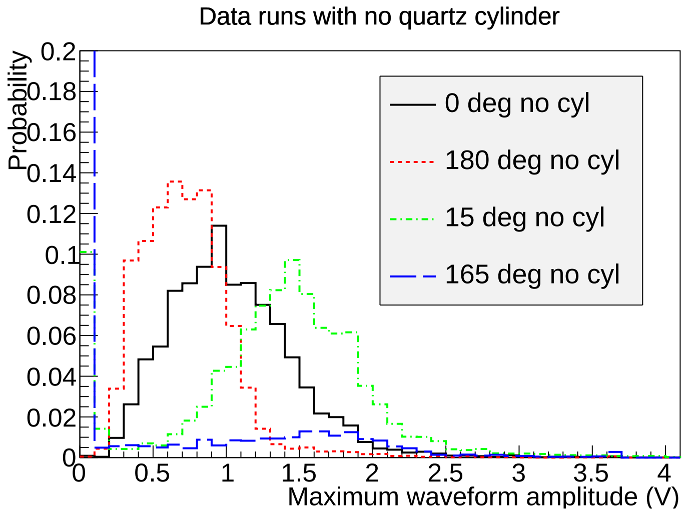

Figure 21: Data collected with quartz cylinder removed in order to determine the contribution of the PMT itself to the signal for low beam angles.

coming and outgoing beams (as explained in the Introduction). Fig. 20 indicates the speed of the Cherenkov signal by two different timing metrics: the main peak full width at half maximum and the jitter in the time of arrival of the Cherenkov signal. In producing the FWHM histogram, a landau fit of main peak was used in order to improve on the 1 ns per point time resolution of the oscilloscope utilized to acquire data. This FWHM histogram indicates that the signals are very fast: a Gaussian fit yields a mean FWHM of 3.09 ns with a sigma of 0.19 ns. The arrival time jitter was calculated by subtracting the interpolated arrival time of the Cherenkov signal from the interpolated arrival time of a trigger scintillator in front of the quartz cylinder. A Gaussian fit indicates that the jitter for this angle has a sigma of 445 picoseconds. The data sets for other angles yielded similarly fast values for both metrics.

Since the time between bunch crossings in the CMS cavern is expected to be 12.5 ns at the Golden Locations, these timing metrics suggest that the Cherenkov signal will be sufficiently fast to allow for discrimination based on timing. This will enable the backwards signal acceptance efficiencies in Fig. 17 to be further decreased.

6.2.3 Low Angle Behavior

Two separate issues will be discussed in this section: (1) the PMT contribution to the signal at low beam angles and (2) the particularly poor directionality of the detector for a beam angle of 0 degrees. Beginning with the first issue, the observation of much larger than expected pulses at low beam angles (namely 0, 15, 165 and 180 degrees) led us to believe that the PMT itself was somehow contributing to the signal. For example, perhaps Cherenkov photons were being produced in the PMT window, which was also made of quartz, and reaching the photocathode with a much higher probability than the Cherenkov photons produced in the quartz cylinder. The exact dimensions of the PMT window are unavailable, but it is known that the window is concave from 1 mm in the center to 8 mm at the edges. Data was collected with just the PMT in the beamline at these low beam angles in order to better understand the signal contribution, if any, from the PMT itself. Fig. 21 displays the results of these tests.

This belief that the PMT itself was responsive for the large signal produced ultimately proved unfounded in that the large signals were in fact a result of the PMT gain being set too high given the number of Cherenkov photons that were produced, but nevertheless carrying out these measurements did yield some unexpected and difficult to interpret results. It is clear that the PMT signal contribution is non-negligible, and it must be carefully considered whether this effect will positively or negatively influence the directionality. If it does in fact have a negative effect, there are two possible courses of action to mitigate the PMT signal contribution: (1) to choose a PMT with as thin a window as possible (if the effect is in fact due to Cherenkov photons being produced in the PMT window) and/or (2) to orient the detector such that the majority of the primary particles will not pass through the PMT.

(Note To Mitch: Mention that there are only advantages to going to a PMT with smaller window, plus it has 4 channels per PMT so we could request a coincidence of two channels in order to reject signals not coming from Cherenkov photons produced by the interaction of a particle in the quartz bar)

Moving on to the second issue, as is evident in Fig. 18), the directionality metric for the 0 degree beam is very poor and does not fit the trend of the previous data points. Some effect must be occurring at the 0 degree beam angle that does not occur at the other beam angles. Looking at the waveform amplitude data from the test beam for all angles makes this evident. The left plot in Fig. 22 shows the angular response of the detector, and it is clear that the 0 degree data displays significantly different behavior than the data for other angles. The trend of lower beam angles producing larger signals (as is expected simply based on the track length of the primary particle through the cylinder being greater for smaller beam angles) is broken by the 0 degree trial. Given the above discussion, one may initially expect that this discrepancy is a function of the PMT signal contribution at low angles. However, this cannot be the case because the PMT signal contribution is approximately symmetric for the 0 degree beam vs, the 180 degree beam, meaning that the amplitude histograms for both the forwards and backwards directions are shifted by a similar amount. Therefore, the overlap between the two histograms should remain relatively unchanged and so there should be no large impact on the final value of the directionality metric.

The true reason for the discrepancy did not become clear until simulations were done. The right plot in Fig. 22 shows output of a simulation of the detector implemented using GEANT4 mimicking the test beam conditions (this simulation is described in detail in Section 6.3). The 0 degree data from the test beam was not reproducible in the simulation until a small air gap was added between the quartz cylinder and the PMT window. Without this air gap, the simulation output for 0 degrees is much higher than the output for 15 degrees These simulation results reveal that the 0 degree signal was much smaller than expected because the angle of many of the Cherenkov photons reaching the end of the cylinder was steep enough that those photons were totally internally reflected back into the cylinder. The Cherenkov photons for the higher beam angles were not affected because their angle with respect to the z-axis of the cylinder was more shallow. The takeaway from this discussion is that the light coupling between the end of the quartz cylinder must be carefully considered for future detector designs.

6.3 Monte Carlo Results

In order to better understand various features of the detector, a model of the detector was developed using GEANT4, a program used to perform Monte Carlo simulations of particle interactions with matter [16]. The ultimate aim of developing the GEANT4 model is to use it to decide upon a particular orientation of the detector within the CMS cavern based on the expected energy and angular distribution of the pp collision products and machine induced background determined from the aforementioned FLUKA simulation.

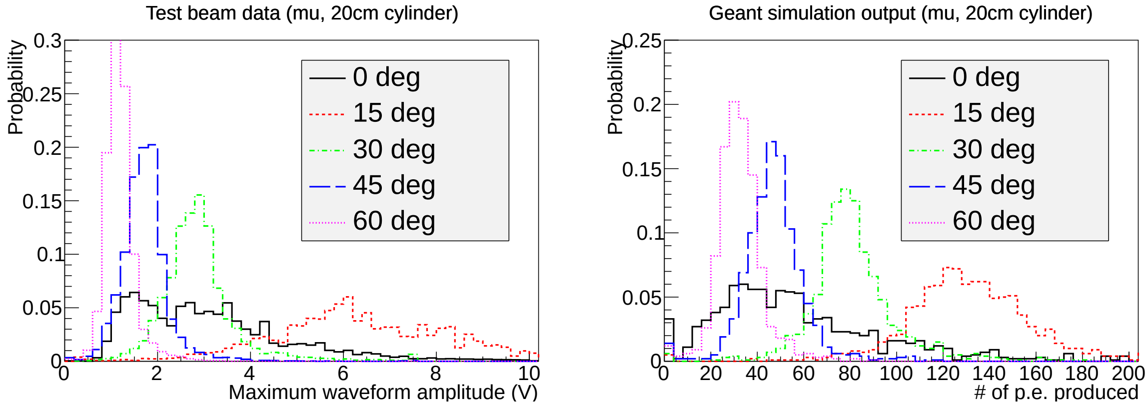

Figure 22: Waveform amplitude histograms constructed from test beam data of relativistic muons incident on a 20 cm quartz cylinder at beam angles of 0, 15, 30, 45 and 60 degrees (Left) and output of a GEANT4 simulation for the same beam parameters.

6.3.1 Simulation Parameters

The Cherenkov process is implemented using code adapted from Example N06, an example program included in the GEANT4 install. Cherenkov photons with wavelengths between 200 and 800 nm are allowed to be generated, and the quantum efficiency of the PMT is applied during photon detection. The initial simulation parameters were set such as to mimic the detector used in and the conditions of the test beam. The detector geometry consists of a polished cylinder of quartz of an adjustable length and radius surrounded by air and encased in a larger cylinder of 2 mm thick aluminum (the shielding). All surfaces of the cylinder are polished and unaltered with the exception of the end cylinder face opposite the PMT which is given a polish of zero (maximum roughness) and defined to be 1% reflective to optical photons of all wavelengths.

6.3.2 Simulation Limitations

Before comparing the simulation output with the data collected in the test beam, various limitations of the model developed must be recognized. Firstly, detailed information about optical properties of the paint used to blackened the end surface of the cylinder was not available. Given the absence of this information, a reflectivity of 1% was chosen, a value which we believe is a conservative upper limit. Secondly, the beam divergence parameters were not precisely known, forcing approximate beam size and dispersion parameters to be chosen. Thirdly, the exact beam energy of the muons at the detector was not know precisely. The beam energy was ultimately approximated by a Gaussian distribution with a sigma of 0.5 GeV centered on 4 GeV. Finally, the exact dimensions of the PMT window are unknown, thus limiting the accuracy to which the PMT can be modelled. Given these limitations, only qualitative agreement between the test beam data and simulation output was sought.

6.3.3 Comparison with Test Beam Data

The purpose of comparing the simulation output to the test beam data was to both better understand what was observed and to validate the simulation. Since the output of the simulation is in units of the number of photoelectrons produced at the PMT photocathode, this had to be appropriately scaled to the test beam data before a comparison could be made. A conversion factor between the number of photoelectrons and the maximum voltage was taken to be the ratio of the most probable number of photoelectrons to the most probable maximum voltage for

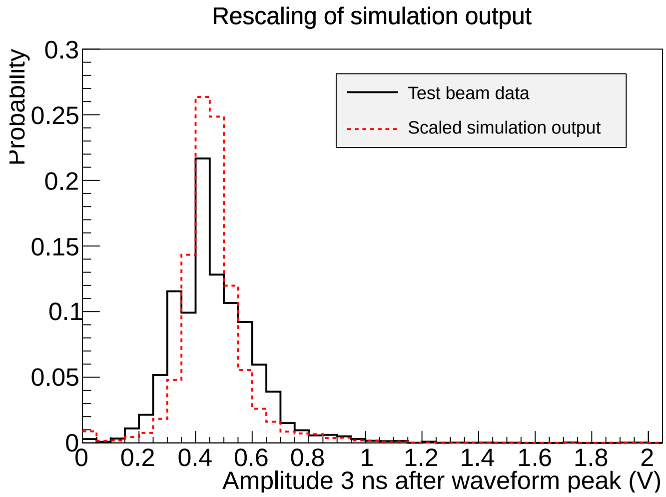

Figure 23: Rescaling of GEANT4 ouput (number of photoelectrons produced in PMT per incident particle) to voltage for 45 degree data.

a single angle. This conversion factor was then kept the same for all other angles. Fig. 23 shows the original and scaled simulation output in comparison with test beam data for a particular beam angle.

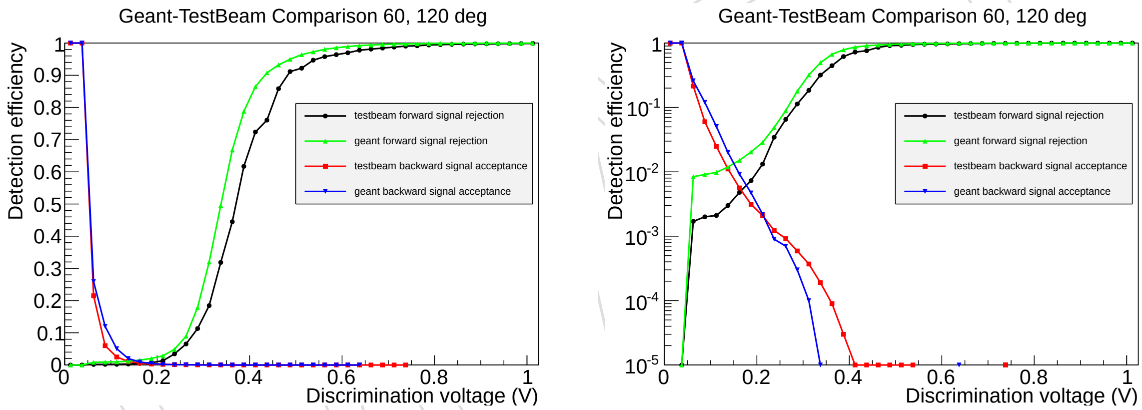

Figure 24: Comparison of detection efficiencies calculated from test beam data to those calculated for rescaled simulation output in linear scale (Left) and logarithmic scale (Right). All plots consist of 10,000 events with the exception of the 120 degree test beam plot which is based on 100,000 events.

Once the scaling is complete, the detection efficiency plots (of which Fig. 17 is an example) can be made for the simulation output and directly compared with the corresponding plots for the test beam data. Fig. 24 shows this sort of comparison for the 60, 120 degree beam angle pair. These results are based on simulations of 10,000 particles passing through the detector for each beam angle. Note the qualitative agreement between the simulation results and the test beam data for both forward and backward beam angles. Given the limitations of the simulation discussed earlier, the visible deviations (especially in the tails of the distribution) are unsurprising. The observed level of agreement is arguably sufficient to consider the simulation validated.

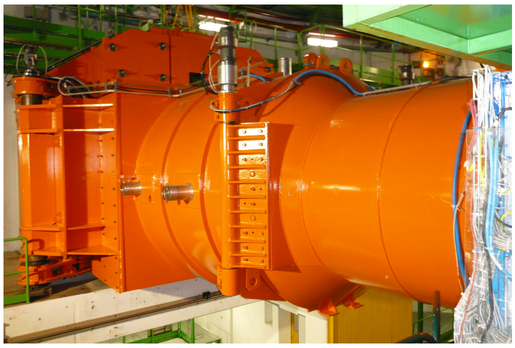

Figure 25: Pictures showing the available space for installation in GL4 (Left) and GL6 (Right).

7 Integration

For the most promising locations (GL4 and GL6), mechanical constraints for a possible installation of our detector were evaluated. The top part of the HF structure is not available, since the whole space is needed for a fast extraction of TOTEM T1, so very limited space is left in GL4 between the outer part of the HF and the green support structure (Fig. 25(Left)). The situation in GL6 (Fig. 25(Right)) looks much more promising, with the only spacial constraint represented by the TAS.

8 Future work

The complete design is expected for Spring 2013. During this time we have to address the following points:

- HF photodetector
- light coupling
- FLUKA identified sources of background
- future test beam studies

References

[1] A. Bell, M. Giunta, A. Benvenuti et al., “BHC Note”, CMS Note 2012/XXX, (2012).

[2] G. Corti and V. Talanov, “Aspects of Machine Induced Backgrounds in the LHC Experiments”, LHC Project workshop Chamonix XV, (2006).

[3] N. Mokhov and T. Weiler, “Machine-induced backgrounds: their origin and loads on ATLAS/CMS”, in *Workshop on Experimental Conditions and Beam Induced Detector Backgrounds, April 3-4 2008, CERN, Switzerland*. Fermilab-Conf-08-147-APC.

[4] R. Bruce, “Machine-induced showers entering the ATLAS and CMS detectors in the LHC”, proceedings of the 2nd International Particle Accelerator Conference, San Sebastian, Spain CERN-ATS-2011-139 ; FERMILAB-Conf-11-393-APC, (4 - 9 Sep 2011).

[5] A. Dabrowski, “The Performance of the Beam Conditions and Radiation Monitoring System of CMS”, proceedings submitted at IEEE Nuclear Science Symposium,Valencia Spain CMS note:CMS CR-2011/275, (Oct. 2011).

[6] A. Bell, “The Design & Construction of the Beam Scintillator Counter for CMS”, master thesis, (2007).

[7] G. Battistoni, S. Muraro, P. Sala et al., “The FLUKA code: Description and benchmarking”, in *Proceedings of the Hadronic Shower Simulation Workshop 2006*. M. Albrow, R. Raja eds., Fermilab 6-8 September 2006. AIP Conference Proceeding 896, 31-49, (2007).

[8] A. Ferrari, P. Sala, A. Fassò et al., “FLUKA: a multi-particle transport code”, *CERN-2005-10 (2005), INFN/TC_05/11, SLAC-R-773*.

[9] K. O. U. TOSCA/OPERA=3d Software, Cobham CTS Limited technical report.

[10] S. Mueller, “The Beam Condition Monitor 2 and the Radiation Environment of the CMS Detector at the LHC”, Technical Report CERN-THESIS-2011-085, (20XX).

[11] N. Mokhov, “The Mars Code System User’s Guide, Fermilab-FN-628 (1995)”,.

N. V. Mokhov and S. I. Striganov, “MARS15 Overview”, in *Proceedings of Hadronic Shower Simulation Workshop*. AIP Conf. Proc. 896, p. 50 (2007), Fermilab, September 2006. Fermilab-Conf-07/008-AD (2007).

[12] G. Robert-Demolaize, “A New Version of SIXTRACK with Collimation and Aperture Interface”, PAC’05, knoxville, tennessee, (2005).

[13] xx, “Heraeus”, Technical Report 20XX/XXX, (20XX).

[14] S. Nag, “Choice of Material for Directional Muon Halo And Measurements of the Signal in a Fused Quartz Bar”, CMS Internal Note 20XX/XXX, (20XX).

[15] xx Technical Report 20XX/XXX, (20XX).

[16] GEANT4 Collaboration Collaboration, “GEANT4: A Simulation toolkit”, *Nucl. Instrum. Meth. A* **506** (2003) 250, `doi:10.1016/S0168-9002(03)01368-8`.

A XXX